Desalination and Water Treatment
www.deswater.com

doi:10.5004/dwt.2018.22749

124 (2018) 37–52
August

Application of factorial design for modeling reverse osmosis process using thin film composite polyamide membrane: a theoretical analysis and experimental validation

Mohamed Mouldi Hamdi[a,*], S. Thiru[a], Lassaad Gzara[b], A.S. Bin Mahfouz[c]

[a]*Mechanical Engineering Department, University of Jeddah, P.O. Box: 80327, Jeddah 21589, Saudi Arabia, Tel. +216 97501500, email: mhamdi1@uj.edu.sa (M.M. Hamdi), thiru@uj.edu.sa (S. Thiru)*
[b]*Center of Excellence in Desalination Technology, King Abdulaziz University, P.O. Box 80200, Jeddah 21589, Saudi Arabia, email: lgzara@kau.edu.sa (L. Gzara)*
[c]*Materials and Chemical Engineering Department, University of Jeddah, P.O. Box: 80327, Jeddah 21589, Saudi Arabia, email: asbinmahfouz@uj.edu.sa (A.S. Bin Mahfouz)*

Received 16 December 2017; Accepted 4 July 2018

ABSTRACT

In this paper, Regression model using a full factorial experimental design with four factors including operating pressure (P_f), salt concentration (C_f), feed flow rate (Q_f), and feed temperature (T_f) at two levels were established to model and optimize the reverse osmosis (RO) process performance. Analysis of variance (ANOVA) technique was used to identify the main and interaction effects of the considered factors on the permeate flux (J_p). Comparisons of model predictions against analytical and experimental data of J_p are analyzed and plotted on 3D response surface and 2D contour plots. The results show that the effect of operating pressure and feed flow rate were significantly influencing factors on the permeate flux at comparatively high feed water temperature and low salt concentration. The chosen model exhibit a satisfactory agreement compared with theoretical and experimental results. An optimal combination of P_f, C_f, Q_f, *and* T_f were found to be 6.3 MPa, 25.6 g/L, 18.0 L/min and 34.6°C, respectively, resulting in a maximum J_p of 44.756 L/h·m^2. Within these optimum conditions, the observed permeate flux is closer to that predicted.

Keywords: Reverse osmosis; Factorial design; ANOVA; Permeate flux; Optimization

1. Introduction

One of the major global challenges today is to reduce the decline in natural fresh water reserves. Numerous countries suffer from a shortage of natural fresh water owing to the global population growth and the increasing demands for water [1]. The water scarcity is also aggravated by the excessive utilization of fresh water in industrial and agricultural activities. Desalination of seawater and brackish water is a significant solution for increasing water demand. Various desalination technologies have been developed to produce fresh water. Multistage flash distillation, multiple effect distillation and vapor compression distillation are the earliest and considerably popular methods of thermal desalination processes [2]. Furthermore, the membrane technologies used for desalination are nano filtration (NF), electro dialysis (ED) and reverse osmosis (RO) processes [3]. Among these desalination processes, RO is one of the substantially promising, widely recognized and used technologies for water desalination [4]. RO is the most used technology to produce fresh water where the RO desalination plants represent more than 50% of the total installed desalination plants worldwide [5,6].

The RO process is basically based on the separation of a dilute solvent from a salt solution using a semi perme-

*Corresponding author.

able membrane that almost allows the molecules of fresh water to totally pass through it from the feed water side to the fresh water side by applying pressure higher than the osmotic pressure of the feed water solution, which depends on the salt concentration [7]. The RO membrane could retain more than 99% of the salt [8] and the osmotic pressure of sea water is approximately 28 bar.

Several transport mechanisms and models have been developed to describe the salt and water permeation through RO membrane. These transport models can be broadly classified into three types: irreversible thermodynamics models, pore-based models and nonporous membrane models such as the solution-diffusion, solution-diffusion-imperfection, and extended solution diffusion models [9]. On the other hand, statistical models have been introduced in order to model, predict, validate and optimize the RO process variables. The statistical models are non-parametric simulative modeling tools known as "black-box" models where all factors vary simultaneously, permitting the study of the interaction effects between the operational variables (operating pressure, flow rate, concentration and temperature) and design variables (dimensions of modules and membrane surface). Unlike the conventional 'one factor at a time' technique, the experiments are generally 'designed' and conducted in a systematic way to develop mathematical models from the experimental data. There are several statistical methods successfully employed in RO process such as factorial design (FD) [10,11], response surface methodology (RSM) [12,13] and artificial neural network (ANN) [14,15].

The literature survey on the modelling of RO process has been exhaustively documented such that virtually most of the possible recorded modelling techniques have been attempted by the researchers and engineers all over the world. However, to the best of the knowledge of the authors, very limited work has been reported on a combined, comparative and comprehensive examination of the theoretical, experimental and statistical models on the performance of the RO process in an integrated manner. An attempt is made therefore to present an extensive, comparative research on the primary process control variables affecting the RO performance theoretically, experimentally and statistically.

In this study, The salt and water permeation through the RO membrane is governed by the solution diffusion transport theory [16,17], whereas a mathematical model based on full factorial design approach is applied to model and optimize the RO process. The statistical method of experimentation are used to understand the interaction effects between the RO performance indicators of the permeate flux and the operational variables such as feed pressure, flow rate, salt concentration and feed temperature. Moreover, comparisons of FFD model predictions against theoretical and experimental results are analyzed and plotted on 3D response surface and 2D contour plots. The major objectives of this study were to:

- identify the independent variables that affect the permeate flux of RO system and conduct preliminary experimentation.
- select the operating limits of the independent variables to conduct preliminary experiments based on full factorial DoE method.
- conduct theoretical calculations to validate and compare the obtained secondary experimental results employing the conventional one factor at a time technique.
- develop mathematical model to identify the main and interaction effects of the independent variables on the response through ANOVA technique and compare the predicted results from the model with the designed experimental results from tertiary experimentation.
- obtain the optimum permeate flux (maximum response point) using desirability function.

2. Description of the RO pilot plant

Fig. 1 shows the schematic diagram of the RO desalination unit. The RO process primarily consists of five major processes. Pretreatment system reduces harmful substances in the feed water before its arrival to the membrane of RO. High-pressure pump, functions to pressurize the preliminary treated water towards the RO modules. Membrane modules consist of four stainless steel pressure vessels containing a spiral wound membrane with multi-stage module arrangement. Post-treatment system consists of sterilization and stabilization of the fresh water. Membrane cleaning system is responsible for regenerating the RO membrane after a long operation time. The production capacity of the RO unit was 0.41 m^3/h and with salinity less than 500 ppm. The technical specifications of main component are given in Table 1.

2.1. Pretreatment system

The pretreatment system was equipped with: i) a raw water intake system and ii) two filtration systems: multimedia sand filter and cartridge filter. The raw water feed tank has a storage capacity of 1 m^3 such that it could sustain a continuous, evenly concentrated solution feed to the RO process for at least an hour at the prescribed experimental conditions. The first step of filtration is the multimedia sand filter. The role of the sand filter is to retain the maximum amount of impurity, sand, dirt and sediments with sizes between 10–50 micron and to reduce the suspended solids and organic matter contained in the feed water. The sand filter is regenerated when the pressure differential exceeds 0.7 bar. The cartridge filter is installed to remove the small amounts of suspended materials escaped from the sand filter. An automatic dosing pump injecting sulfuric acid is installed prior to the filters to adjust the pH and for scale prevention. A feed water pump of 0.28 kW absorbed power transfers the feed water to the RO membrane modules.

2.2. High pressure pump (HPP)

The HPP (CAT pumps, type 661) used in this study is a high efficiency plunger pump of 2.53 kW absorbed power. The maximum operating pressure and flow capacity of the pump is 210 bar and 2.27 m^3/h, respectively. A pulsation dampener is installed on the pump discharge line to dampen the pressure variations and for smooth operation. It is used to force the water through the membrane modules and to supply the required pressure and feed flow rate.

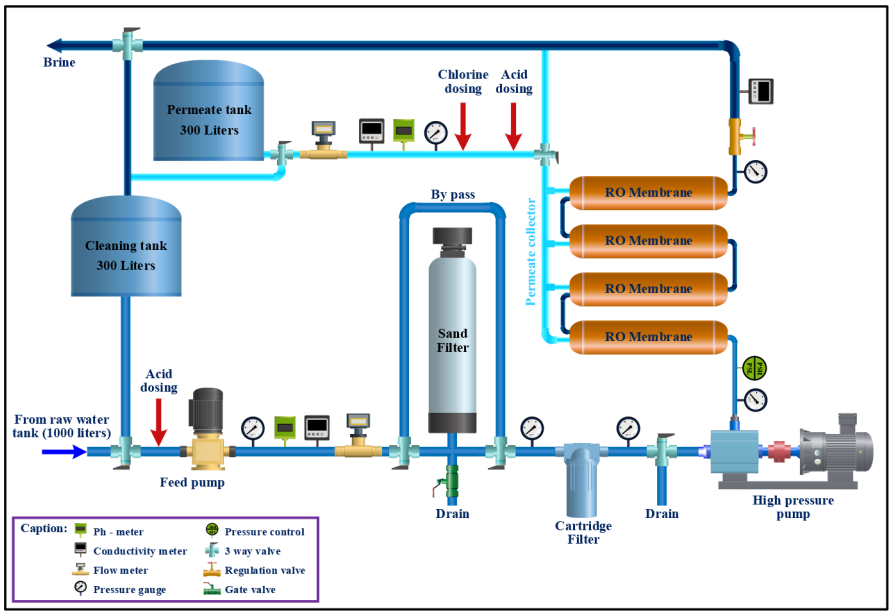

Fig. 1. Schematic diagram of the RO desalination unit.

Table 1
Technical specification of main component of the RO desalination process

Item	Specifications
Filmtec membrane	Membrane type: thin-film composite
	Membrane material: polyamide - PA
	Active area: 2.8 m^2
	Element configuration: Spiral wound
	Number of RO modules: 4 vessels in series
	2 spiral-wound elements
HHP	Model: CAT Pumps / Model 661
	Max flow: 38 l/min
	Min pressure: 100 psi, (7 bar)
	Max pressure: 3000 psi, (210 bar)
	Hydraulic efficiency: 0.92
	Motor efficiency: 0.8
Feed pump	Model: GRUNDFOS, CRNI-8
	Nominal power: 0.55 kW
	Flow: 1.8 $m^3 \cdot h^{-1}$
	Head: 35.9 m
	Hydraulic efficiency: 0.50
	Motor efficiency flow through pump: 0.85

2.3. Membrane modules

The designed RO unit consists of polyamide thin film composite spiral wound seawater reverse osmosis membranes. The membrane element used was 2.5" Film-Tec, SW30-2540 with 99.4% salt rejection and active surface areas of 2.8 m^2. The membrane racks consist of 4 pressure vessels each containing 2 spiral-wound elements. In order to increase the overall system recovery ratio of about 40% and the total permeate flow of 0.41 m^3/h, the concentrate staging configuration was employed as shown in Fig. 1. This arrangement operate with the principle of the concentrate from the first stage becomes the feed to the second stage [18].

2.4. Post treatment system

The water produced from a RO membrane in major cases requires certain form of post treatment. The product water is treated and continuously monitored by the addition of caustic soda for pH adjustment and by the addition of chlorine for sterilization.

2.5. Cleaning system

An integrated membrane cleaning system including a cleaning tank is used when the productivity and salt rejection decreases and the pressure increases. A high-level flush tank is integrated in the unit to provide a fresh water supply for flushing during the shutdown.

2.6. Measurements and control

The RO unit is equipped with the measurements equipment and control systems for monitoring various operation variables. The pH indicator is mounted on the feed line to measure the pH of the feed water before entering the filters. Conductivity meter is installed on the permeate line and the brine line to determine the product water quality and salt rejection. In addition, an alarm is used to signal the permeate loss. Flow meters are used to measure permeate and brine flow rates. Pressure gauges are installed at different positions to measure the pressure drop across the filters, pump inlet and discharge pressures, operating pressure to the membrane elements, pressure drop across membrane element, concentrate and the permeate. Pres-

sure shutdown switches are located on either side of the high-pressure pump to trip on low suction pressure and excessive delivery pressure, as well as on the permeate delivery line to avoid the pressurization of the low product system. A high temperature switch is used for membrane protection. A flow control valve in the brine line is used to set the required recovery. A relief valve is installed in the discharge line of HPP to control the operating pressure to the membrane module. Also, a three-way valve to direct the product water to the drain if salinity > 500 ppm.

3. Water transport equation

The solution diffusion model governs the mechanism of mass transfer through nonporous reverse osmosis membrane. The solvent flux depends on pressure differences across the membrane thin film. Whereas, the driving force for the solute passage on membrane surfaces is provided by diffusion due to concentration differences [19]. In reverse osmosis the solution diffusion model, film theory, and the laws of energy and mass conservation were employed to determine the permeate flux of the RO processes [20].

Table 2
Water transport equations

Parameters	Equations	References	
Permeate flux	$J_p = \frac{Q_p}{S} = A_p(\Delta P - \Delta\pi)$	(1)	[21,22]
Solute flux	$J_s = B_s(C_m - C_p)$	(2)	[22,23]
Water permeability coef.	$A_p = A_{p0}\exp\left(1965\left(\frac{1}{298} - \frac{1}{273.15 + T_f}\right)\right)$	(3)	[23,24]
Salt permeability coef.	$B_s = B_{s0}\exp\left(\alpha\frac{T_f - 273}{273}\right)$	(4)	[23,24]
Osmotic pressure	$\Delta\pi = RT_f(C_m - C_p)$	(5)	[24]
Concentration polarization	$CP = \frac{C_m - C_p}{C_b - C_p} = \exp\left(\frac{J_p}{k_c}\right)$	(6)	[16,22]
Mass transfer coefficient	$k_c = Sh\frac{D_{AB}}{d_h} = 0.065Re^{0.875}Sc^{0.25}\frac{D_{AB}}{d_h}$	(7)	[25]
Reynolds number	$Re = \frac{\rho d_h u}{\mu}$	(8)	[23]
Diffusion coefficient	$D_{AB} = 6.725\cdot10^{-6}\exp\left(0.1546\cdot10^{-3}C_b - \frac{2513}{273.15 + T_f}\right)$	(9)	[23,26]
Dynamic viscosity	$\mu = 1.234\cdot10^{-6}\exp\left(0.00212C_b + \frac{1965}{273.15 + T_f}\right)$	(10)	[23,26]
Density of feed	$\rho = 498.4M + \sqrt{248400M^2 + 752.4MC_b}$	(11)	[23,26]
Constant	$M = 1.0069 - 2.757\cdot10^{-4}T_f$	(12)	[23,26]
Flow balance	$Q_f = Q_b + Q_p$	(14)	[22]
Mass balance	$Q_fC_f = Q_bC_b + Q_pC_p$	(13)	[27]
Recovery ratio %	$RR = \left(\frac{Q_p}{Q_f}\right)\times100$	(15)	[27]
Salt rejection	$SR = \left(1 - \frac{C_p}{C_f}\right)\times100$	(16)	[28]

Table 2 illustrates the equations describing the reverse osmosis modeling.

4. Experimental design and data analysis

4.1. Limits of operating variables variation for the factorial design analysis

The effect of P_f on permeate flux at different C_f is shown in Fig. 2a. For P_f ranging from 4.6 MPa to 5.2 MPa, in the lower pressure region, the J_p increases exponentially. Whereas, in the higher pressure region, above 5.2 MPa, the J_p increases linearly that illustrates a linear relationship between the J_p and the P_f. Fig. 2(b) illustrates the permeate flux dependence on the Q_f at different T_f ranging from 14.9°C to 34.6°C at constant P_f of 6.3 MPa. The variation of J_p against Q_f demonstrates an exponential curve in the low Q_f variation from 4 L/min to 10 L/min, and thereafter a gradual linear increase is observed in the range of Q_f from 10 L/min to 18 L/min. Fig. 2c illustrates the effect of T_f on the permeate flux. The curves demonstrate a considerable linear increase trend with J_p. For a constant Q_f, C_f and given P_f of 18 L/min, 36.2 g/L and 6.3 MPa, respectively, the J_p increased from 24.5 L/h.m² to 33.1 L/h.m² when the T_f increased from 14.9°C to 34.6°C, respectively. The effect of C_f on the permeate flux is illustrated in Fig. 2(d). The permeate flux decreases gradually to attain a minimum of 33.0 L/h·m², for a Q_f of 18 L/min at constant T_f of 34.6°C. The C_f demonstrates a diminishing nonlinear relationship with the J_p at its lower range (from 16.3 g/L to 25.6 g/L). Evidently, beyond this range the curves demonstrate a linear relationship between the J_p and C_f.

From these results, it is observed that there is a region where P_f, C_f, Q_f *and* T_f have linear relationships with the permeate flux. Therefore, the range of variables is provided in Table 3.

4.2. Full factorial design methodology

In the present study, a two-level-four-factor full factorial experimental design was carried out to model and optimize permeate flux. The procedure for the suggested methodology is represented in the form of a flowchart as shown in Fig. 3. In a two-level-four-factor FFD, the minimum number of experimental runs requires being $2^4 = 16$ runs replicated twice. The four independent factors, P_f, C_f, Q_f *and* T_f were studied at two levels, a 'low' and a 'high' level. The low level and the high level of each factor were coded as (–1) and (+1) respectively. The experimental range and coded levels of the independent factors are given in Table 4.

The statistical and graphical analysis of experimental data was performed using statistical and graphical analysis MINITAB® software release 17 developed by Minitab Inc., USA [29]. This software was used for regression analysis of the data obtained and to identify the main and interaction effects between the various operating variables and their

Table 3
Upper and lower limit of operating variables

Parameters	P_f [MPa]	C_f [g/L]	Q_f [L/min]	T_f [°C]
Lower limit	5.2	25.6	10.0	14.9
Upper limit	6.3	36.2	18.0	34.6

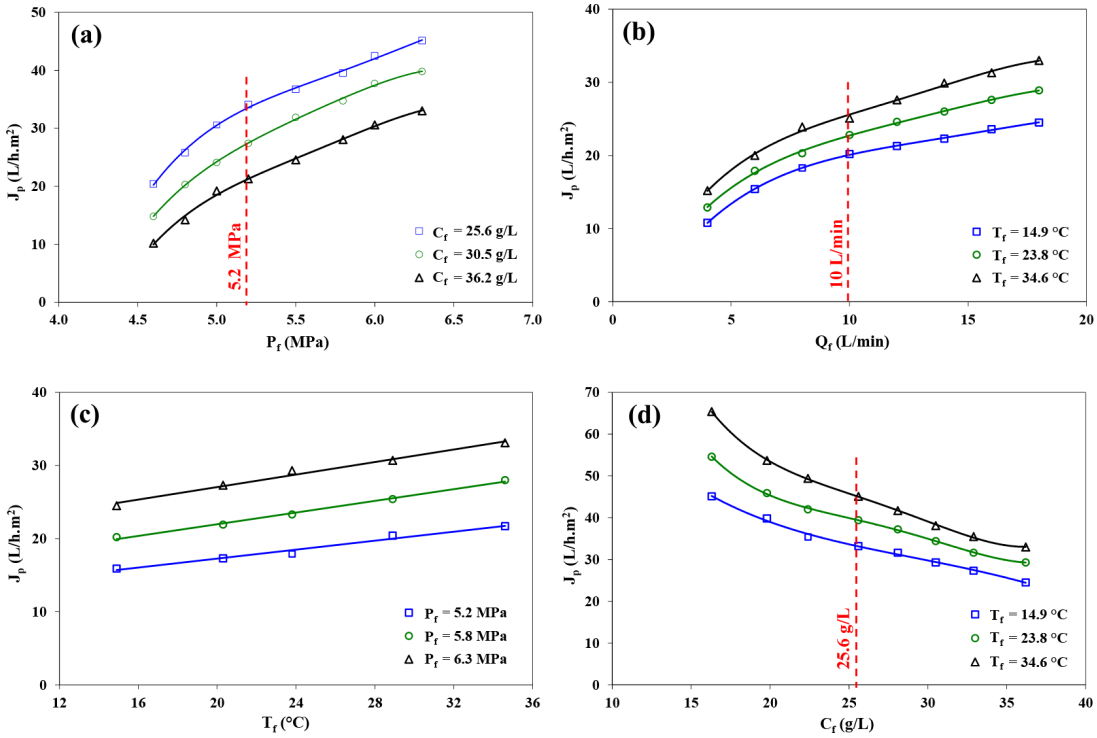

Fig. 2. Effect of operating variables: (a) J_p vs. P_f, (b) J_p vs. Q_f, (c) J_p vs. T_f and J_p vs. C_f.

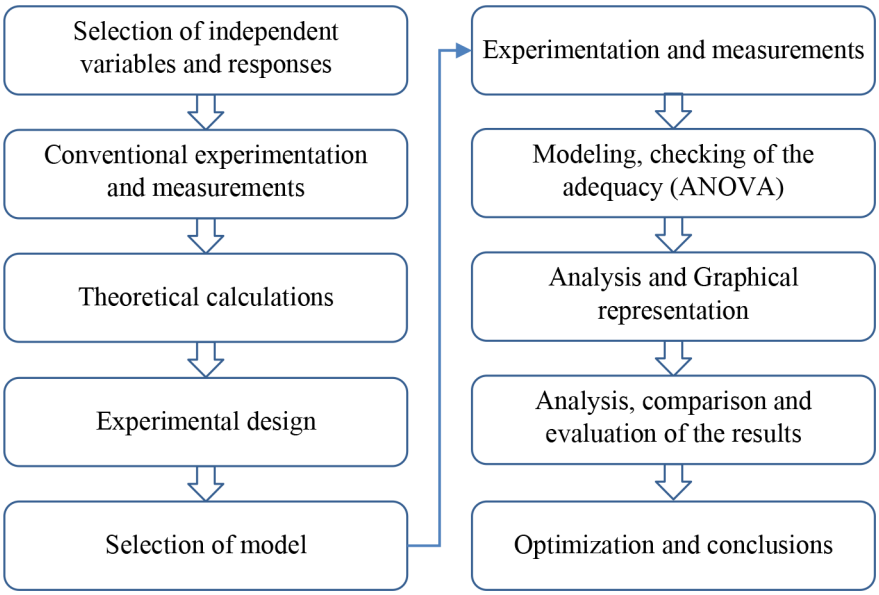

Fig. 3. Flowchart of the model procedure.

Table 4
Control parameters and their limits

Parameters	Unit	Parameters symbol	Coded symbol	Actual value of coded levels	
				Low (–1)	High (+1)
Operating pressure	MPa	P_f	$\beta 1$	5.2	6.3
Salt concentration	g/L	C_f	$\beta 2$	25.6	36.2
Feed flow rate	L/min	Q_f	$\beta 3$	10.0	18.0
Feed temperature	°C	T_f	$\beta 4$	14.9	34.6

influences on the predicted response (J_p) through ANOVA technique. The design matrix for the replicated 48 test runs prescribed by Minitab17® software and the data obtained from the experiments are illustrated in Table 5. The linear regression equation based on the first-order model with four parameters and all their two-way interaction terms can be given in the form of the following equation [30]:

$$Y = \beta_0 + \sum_{i=1}^{k} \beta_i X_i + \sum_{1 \le i \le j}^{k} \beta_{ij} X_i X_j + \varepsilon \quad (1)$$

where Y is the predicted response, k is the number of factors, β_0 is the constant term, β_i is the linear coefficient representing the effect of the factor, β_{ij} represents the interaction effects, X_i and X_j are the independent coded variables, and ε is the experimental error.

For the present work, the linear regression equation was obtained using the coded independent parameters as the following:

$$J_p = \beta_o + \beta_1 P_f + \beta_2 C_f + \beta_3 Q_f + \beta_4 T_f + \beta_{12} P_f C_f + \beta_{13} P_f T_f + \beta_{23} C_f Q_f + \beta_{24} C_f T_f + \beta_{34} Q_f T_f \quad (2)$$

where J_p is the permeate flux, β_0, β_1, β_2, β_3, β_4 are the linear coefficients and β_{12}, β_{13}, β_{14}, β_{23}, β_{24}, β_{34} are the second order interaction terms.

5. Results and discussion

5.1. Modeling and statistical analysis

The experiments were conducted in random order as per the design matrix shown in Table 5. A regression analysis was conducted for the collected experimental data to fit a linear model using the least square technique. The developed mathematical model for predicting the permeate flux as the response from the design matrix based experimentation results determined in Table 5 is expressed in terms of actual parameters and can be written as follows:

$$J_p = 25.683 + 4.256P_f - 4.310C_f + 3.158Q_f + 3.485T_f + \beta 12 P_f C_f + 0.163 P_f C_f + 0.722 P_f Q_f + 0.276 P_f T_f + 0.827 C_f Q_f - 0.506 C_f T_f + 0.936 Q_f T_f \quad (3)$$

The primary effects of the factors were identified by the statistical significance of fitted models based on the Fisher's exact test (p-value < 0.05) of confidence intervals using the ANOVA methodology. The model adequacy and error independency for each variable were used to diagnose the fitted models. The ideal developed model was evaluated by coefficient of determination (R^2). The normality of the errors was checked by statistical analysis through normal probability plot of the empirical data in terms of the standardized

Table 5
Design matrix for experimentation and results

Standard order	Parameters (input variables)				Permeate flux: J_p (L/h·m²)			
	P_f	C_f	Q_f	T_f	Experimental			Predicted
1	− 1	− 1	− 1	− 1	20.1	20.3	19.8	20.1
2	+ 1	− 1	− 1	− 1	26.6	26.5	27.0	26.7
3	− 1	+ 1	− 1	− 1	13.1	12.6	12.5	12.7
4	+ 1	+ 1	− 1	− 1	20.2	20.7	20.4	20.4
5	− 1	− 1	+ 1	− 1	24.4	24.2	23.9	24.2
6	+ 1	− 1	+ 1	− 1	33.2	32.9	33.1	33.1
7	− 1	+ 1	+ 1	− 1	15.9	16.0	15.9	15.9
8	+ 1	+ 1	+ 1	− 1	24.5	24.3	24.7	24.5
9	− 1	− 1	− 1	+ 1	25.0	25.6	25.8	25.5
10	+ 1	− 1	− 1	+ 1	31.9	32.0	31.5	31.8
11	− 1	+ 1	− 1	+ 1	17.7	17.7	17.8	17.7
12	+ 1	+ 1	− 1	+ 1	25.1	25.2	25.6	25.3
13	− 1	− 1	+ 1	+ 1	34.1	33.7	34.0	33.9
14	+ 1	− 1	+ 1	+ 1	45.1	44.5	44.7	44.8
15	− 1	+ 1	+ 1	+ 1	21.3	21.7	21.3	21.4
16	+ 1	+ 1	+ 1	+ 1	33.0	32.8	33.1	32.9

Table 6
ANOVA results for J_p

Source	Sum of squares	Degree of freedom	Mean square	F_p value	p-value Prob > F_p
Model	2822.91	4	705.728	11790.76	< 0.0001
A - P_f	869.43	1	869.4305	14525.77	< 0.0001
B - C_f	891.61	1	891.610	14896.33	< 0.0001
C - Q_f	478.74	1	478.736	7998.35	< 0.0001
D - T_f	583.14	1	583.135	9742.57	< 0.0001
AB	1.27	1	1.274	21.29	< 0.0001
AC	25.05	1	25.054	418.59	< 0.0001
AD	3.66	1	3.658	61.11	< 0.0001
BC	32.83	1	32.829	548.49	< 0.0001
BD	12.27	1	12.269	204.99	< 0.0001
CD	42.09	1	42.087	703.16	< 0.0001
Pure Error	1.92	32			
Cor Total	2957.38	47			

R^2 = 0.9994, Adjusted R^2 = 0.9990, Predicted R^2 = 0.9985

residuals. The software allowed obtaining of the statistical parameters; Pareto chart and interaction effect plots that aided in identifying the parameter conditions for optimal permeate flux.

5.2. Validation of the model through ANOVA

The adequacy and the significance of each coefficient for the developed model were tested by applying the ANOVA technique. The standard error of estimated (SE) coefficient of multiple correlations and coefficient of determination (R^2) for all major effects and two-way interactions generated from the regression analysis are illustrated in Table 6. The significance is evaluated as p-value, the probability value used to determine the effect in the model that was statistically significant [30]. Based on the p-values that are less than 0.05, it was found that all the terms in the model have significant effects on the response. Therefore, the individual effect of each of the significant parameters (P_f, C_f, Q_f *and* T_f) on permeate flux does change in the presence of the other factors.

The effects of the considered parameters and their interactions on the response are presented in a Pareto chart shown as Fig. 4. The Pareto chart presents the absolute values of the effects of main parameters and the effects of interaction of factors [31], and is illustrated as horizontal bars.

The tall bar in the plot represents the substantially important factor; the one that follows the most important factor is represented by next tallest bar, and so on. To indicate the potentially important factor, a reference line is drawn such that the factors that extend past this line are statistically significant [31] at 95% confidence level.

It could be confirmed from the Pareto chart that all analyzed effects are statistically significant. The C_f has the significantly high effect followed by P_f, T_f and Q_f. The relative importance of the combination of factors could also be observed from the Pareto chart.

5.3. Interaction effects plot

Fig. 5 shows the two-way interaction effects plot for the permeate flux. Among the four input parameters considered for the study viz., P_f, C_f, Q_f *and* T_f, and the two parameter combinations, Q_fT_f has prominent positive interaction effect followed by P_fQ_f on permeate flux. However, the C_fQ_f has strong negative interaction effect followed by C_fT_f on J_p. The P_fT_f has moderate positive interaction effect and P_fC_f has minimum interaction effect on J_p. Fig. 5 evidently indicates that the salt concentration has affected the permeate flux individually as a main factor not only by decreasing it, but also by interacting with Q_f and T_f to reduce it further. However, the slight interaction of C_f with P_f caused positive effect on permeates by a comparatively small (minimum) increment. The two-way interaction plot therefore is an indicator of the negative impact of salt concentration that could be countered by increasing the Q_f and T_f in RO process.

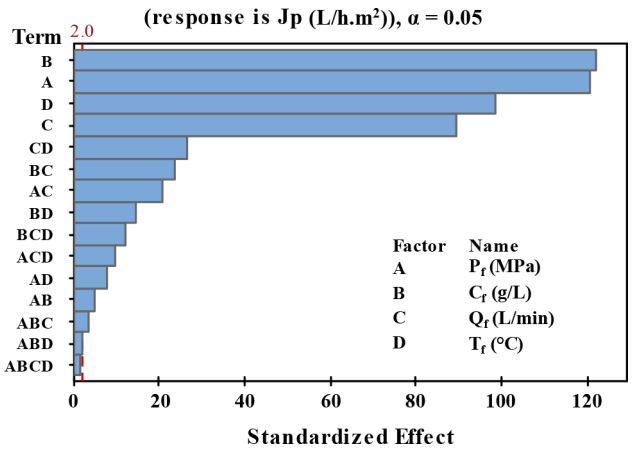

Fig. 4. Pareto chart of the standardized effects.

5.4. Comparison of model predictions against analytical and experimental data

In this study, the experimental and theoretical results of the permeate flux versus the operating variables of T_f, Q_f, C_f *and* P_f are investigated and represented on 3D response surface and 2D contour plots in Figs. 6a–11a. The experiments were conducted by varying the operating variables of operating pressure, feed flow rate, feed temperature and salt concentration of 5.2–6.3 MPa, 10–18 L/min, 14.9–34.6°C and 25.6–36.2 g/L, respectively. The graphical representation of the model for predicting the permeate flux under the effect of these operating variables are illustrated in Figs. 6b–11b.

5.4.1. Dependence of permeate flux on feed flow rate and feed temperature

Fig. 6 depicts the interaction and combined effect of feed flow rate and feed temperature on the permeate flux in the three-dimensional (3D) surface plots and contour plots. Although most of the real desalination processes are conducted at a constant temperature, the influence of T_f on J_p was mainly considered in this study to validate model prediction and optimize the response. The experimental results

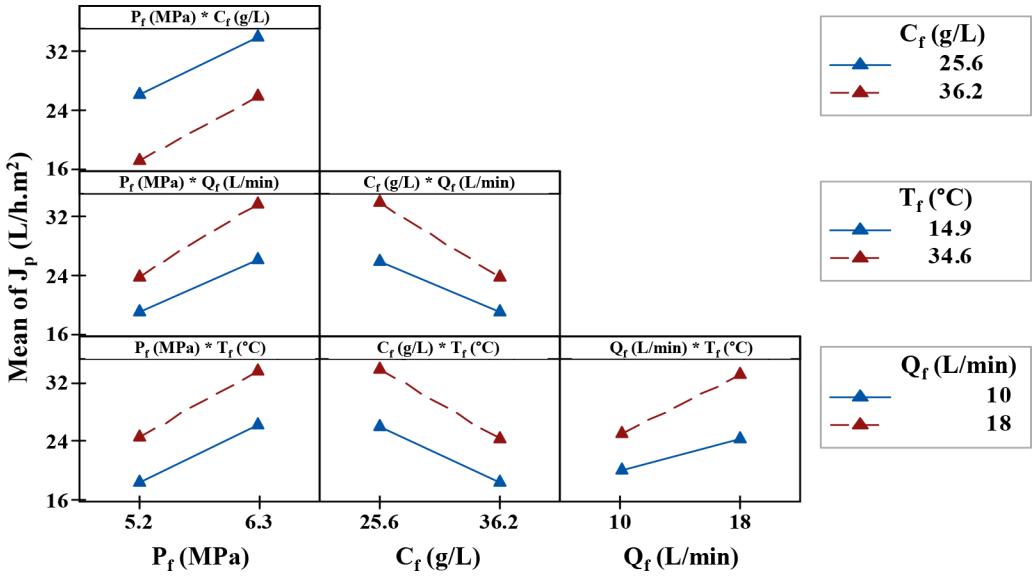

Fig. 5. Interaction plots for statistically predicted J_p.

of the effect of Q_f and T_f on permeate flux are compared with the theoretical values, illustrated in Fig. 6a. Whereas, Fig. 6b demonstrates the response surface and contour plot of the prediction model for permeate flux. It could be observed from these results that the permeate flux increases significantly with increase in both the feed flow rate and feed temperature. It was observed from the experimental and theoretical results that the permeate flux attains a maximum value of 33.0 L/h·m² and 32.7 L/h·m², respectively at higher feed flow rate of 18 L/min and higher feed temperature of 34.6°C. A maximum value of permeate flux of 32.8 L/h·m² was determined by the regression model. These results indicate a satisfactory agreement, when comparing the experimental and the theoretical results with the model predictions. Thereby, the contour plots of Fig. 6a demonstrate that the interaction between the experimental and the theoretical results follow a similar trend.

The positive impact of increasing both the feed flow rate and feed temperature on the permeate flux are due to the increase of Reynolds number (according to Eq. (8)) and to the increase in the diffusion coefficient. Suhan and Eric [20], reported that the turbulent flows enhance mass transfer that causes a comparatively small concentration polarization on the surface of membrane and lower osmotic pressure drop resulting in a comparatively large relative permeate flux. Comparatively high Reynolds number and the sweep of the feed water on the membrane surface result in the decrease of the accumulated solute, reduction of the hydraulic resistance of the 'cake' and the thickness of the boundary layer [32]. Also, the increase in feed temperature at the feed side improves the water permeability coefficient (refer to Eq. (3)) and decreases the density and viscosity of the feed water. A comparatively high T_f could affect the structure and morphology of membrane by increasing the membrane pore size and the diffusivity coefficient that leads to the enhancement of J_p [33,34].

Further, as it can be seen from the contour plot of Fig. 6a that the trend of the theoretical calculations presents a small deviation (about 3.0%) with the experimental results. This deviation was illustrated at lower and higher values of T_f, suggesting enhanced solute accumulation at the membrane surface and also may be due to changes in the physical properties of the polymeric membrane.

5.4.2. Dependence of permeate flux on operating pressure and salt concentration

The effects of operating pressure on permeate flux at different salt concentration values are illustrated on the 3D surface plot and 2D contour plot in Figs. 7a and 7b respectively. The 3D surface plot and 2D contour plot for the correlation between the experimentally obtained and theoretically calculated values of the change of the permeate flux at different operating pressures and salt concentrations are shown in Fig. 7a. At lowest salt concentration, it was experimentally proven that the actual permeate flux increased from 34.1 L/h·m² to 45.1 L/h·m² when the operating pressure ranged from 5.2 bar to 6.3 bar, respectively whereas, the calculated permeate flux is observed to range from 34.3 L/h·m² to 47.5 L/h·m² with the same operating pressure range. The graphical representation of the model for predicting the permeate flux using Eq. (19) is illustrated in Fig. 7b. From this curve, it is observed that the operating pressure has a positive effect whereas salt

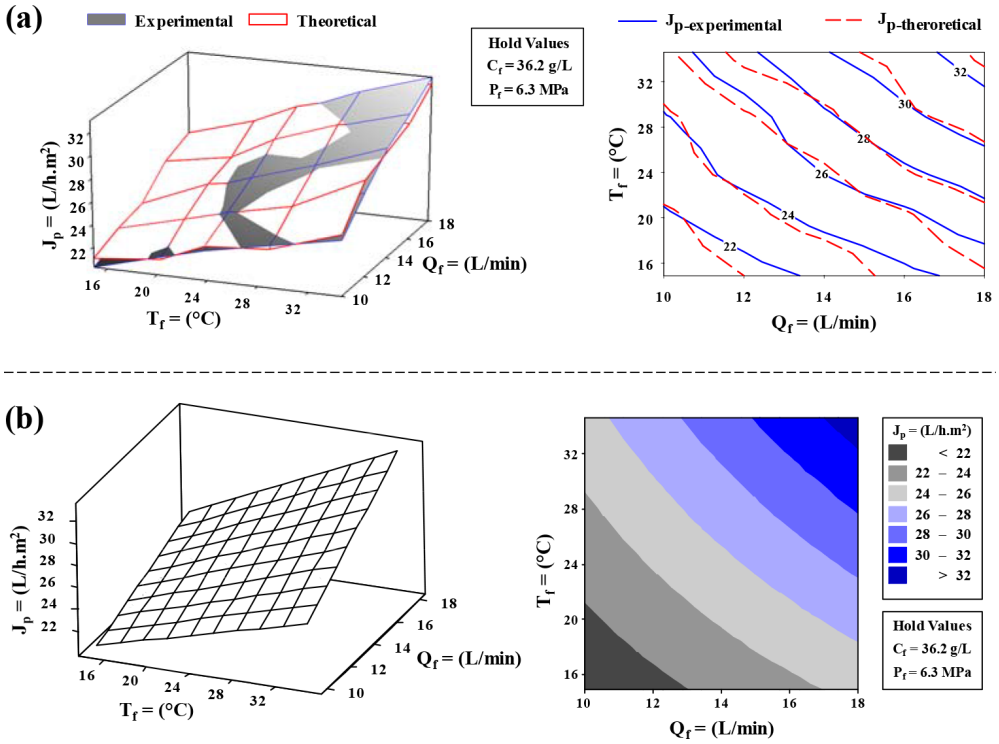

Fig. 6. 3D response surface and 2D contour plots of permeate flux as a function of Q_f *and* T_f: (a) Experimental and theoretical J_p, (b) Statistically predicted J_p.

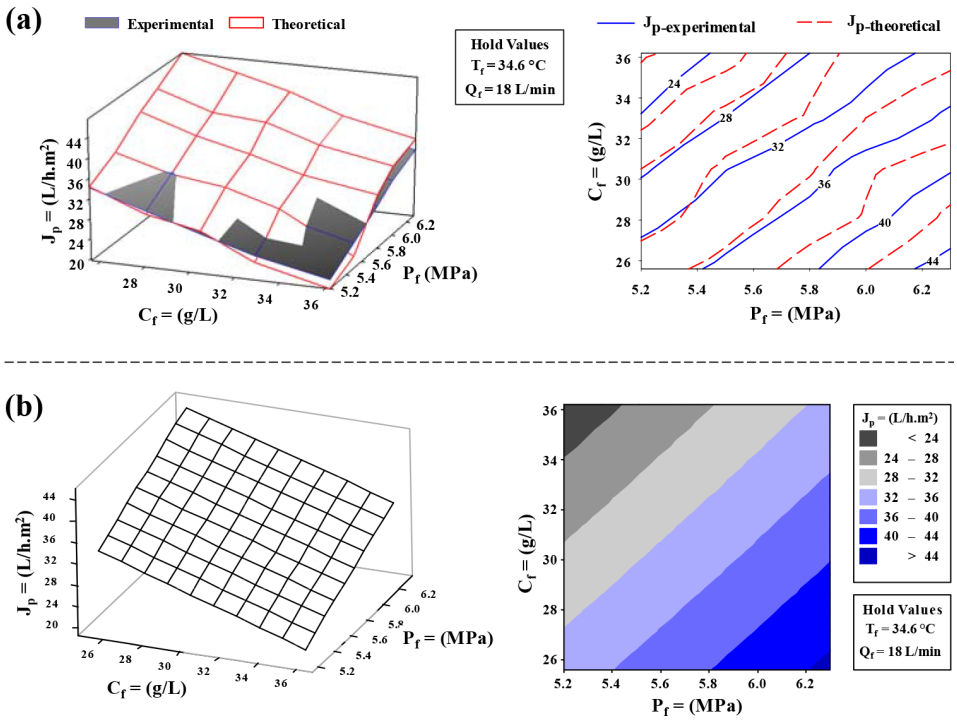

Fig. 7. 3D response surface and 2D contour plots of permeate flux as a function of P_f *and* C_f: (a) Experimental and theoretical J_p, (b) Statistically predicted J_p.

concentration has a negative effect on the prediction model of permeate flux. From these results, it could be noted that an increase in the operating pressure increases the permeate flux, but as the salt concentration was increased the permeate flux decreased as expected. It could be observed that for a constant T_f and Q_f maintained at 34.6°C and 18 L/min respectively, the permeate flux has direct relationship with operating pressure and an inverse relationship with salt concentration. The permeate flux attains its highest point when the C_f is at its lowest value (25.6 g/L) and correspondingly at the highest P_f (6.3 MPa). The combined effect of high operating pressure and low salt concentration results in the increase of driving force for water permeability (refer to Eq. (1)) and decrease of osmotic pressure (according to Eq. (5)). Moreover, the mass transfer coefficient and the membrane permeability are exceedingly sensitive to the salt concentration and decrease significantly at comparatively high values of C_f [35]. Further, it is evidently observed from the contour plot that the trend of the theoretical calculations present a small deviation (approximately 4.8%) with the experimental results. This percent error was registered at the high permeate flux values that could be created owing to the required low transmembrane pressures caused by the increase in driving force. In addition, the permeate flux could be affected by the concentration polarization of solute at the membrane surface that causes considerable resistance of the membrane [36].

5.4.3. Dependence of permeate flux on operating pressure and feed temperature

Figs. 8a and 8b illustrate the change in permeate flux at different operating pressures and feed temperatures with constant salt concentration of 36.2 g/L and constant feed flow rate of 18 L/min. Fig. 8a demonstrates comparisons of theoretical and experimental permeate flux, while Fig. 8b illustrates the graphical representation provided by the mathematical model. These results indicate that the flux of the RO membrane increases with an increase of operating pressure and temperature and attains maximum values of 33.1 and 33.6 L/h·m² for experimental results and theoretical calculations, respectively. A maximum value of 33.0 L/h·m² of permeate flux was determined by the mathematical model. When P_f ranges from 5.2 MPa to 6.3 MPa at T_f = 14.9°C the experimental permeate flux changes from 15.9 L/h·m² to 24.5 L/h·m², whereas it ranges from 15.9 L/h·m² to 21.7 L/h·m² when T_f ranges from 14.9°C to 34.6°C maintaining a constant P_f of 5.2 MPa. From these results, it is evident that the effect of operating pressure is comparatively more significant and important than that of the feed temperature on permeate flux. It could be observed from contour plots that the effect of pressure is considerably more significant at comparatively higher temperatures. The reasons behind the enhancement of the permeate flux with increasing pressure and temperature might be related to the change of the properties and morphology of the membrane. In general, when the feed temperature increases the concentration polarization reduces (according to Eq. (6)) while the mass transfer improves [Eq. (7)] [34,37]. A comparatively higher temperature increases the membrane permeability caused by the reduction in water viscosity (refer to Eq. (10)) and the increases of the solubility of water in the membrane and consequently enhances the diffusion coefficient leading to the increase of the water permeability [38]. The increase of J_p with respect to operating pressure might occur owing to the rapid increase in water activity [39]. The contour plot

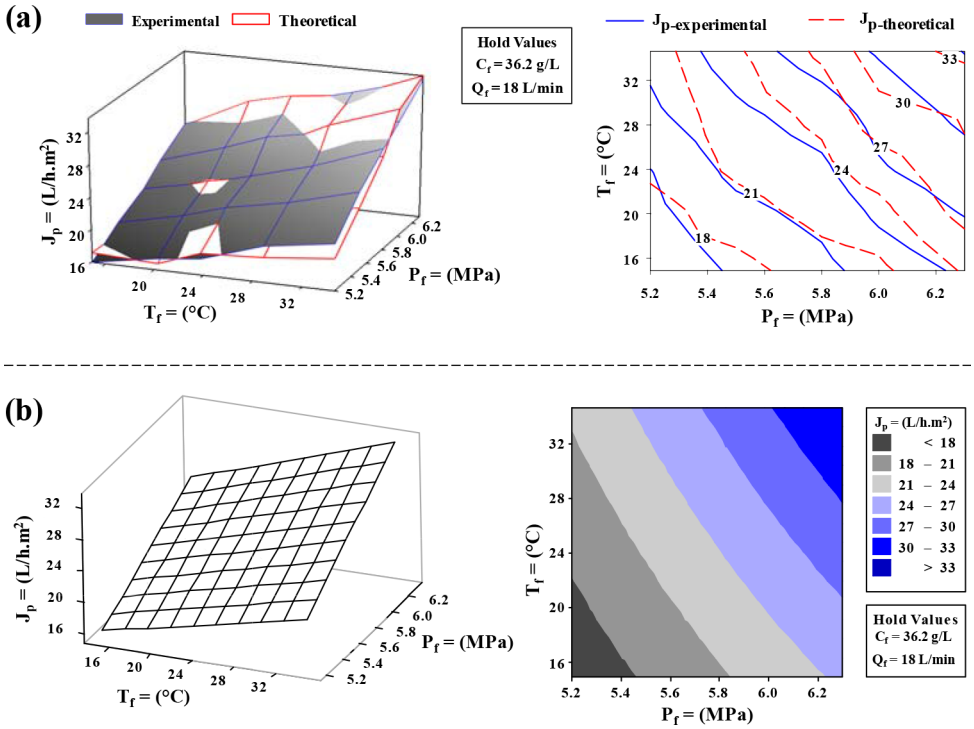

Fig. 8. 3D response surface and 2D contour plots of permeate flux as a function of P_f *and* T_f: (a) Experimental and theoretical J_p, (b) Statistically predicted J_p.

illustrates a small difference between the measured results and the theoretical calculations, with an error of approximately 4.1%. This percentage difference is observed at the lowest and highest values of temperature. The lowest operating temperature results in the stiffness of the membrane matrix that leads to the changes in the physical properties of the membrane materials [40]. Furthermore, substantial pressure could cause the hardening of membrane, known as the phenomenon of mechanical compaction [41].

5.4.4. Dependence of permeate flux on feed flow rate and operating pressure

Fig. 9a illustrates the comparisons between the variations of permeate flux determined experimentally and calculated theoretically as a function of feed flow rate and operating pressure. Fig. 9b illustrates the 3-dimensional response surface and the corresponding contour plots of permeate flux versus the two afore-mentioned varying parameters. It is observed that a gradual increase in the Q_f *and* P_f, leads to a rapid increase of the permeate flux of the RO membrane. The response surface and contour plot demonstrate that the highest flux values were achieved when the flow rate was approximately 18 L/min and the operating pressure was approximately 6.3 MPa. At the same operating conditions as mentioned above and with 36.2 g/L salt concentration and 34.6°C feed temperature, the highest permeate flux obtained experimentally and theoretically were 33.0 and 34.3 L/h·m², respectively. It could be observed from the graphical representation of the model that the predicted permeate flux increases from 25.1 to 33.0 L/h·m², which is a 31.5% increase as the feed flow rate increases from 10 to 18 L/min when operating pressure is maintained constant at 6.3 MPa. As the operating pressure was increased from 5.2 to 6.3 MPa at constant feed flow rate of 18 L/min, the predicted permeate flux was enhanced from 21.3 to 33.0 L/h·m², which was a 55% increase. From the results, it could be noted that the influence of operating pressure appears to be more significant than that of feed flow rate for permeate flux at the prescribed condition and the operating pressure provides a major impact on the prediction model of permeate flux. The contour plot illustrates an average difference of 3.7% between the permeate flux obtained experimentally and that calculated at different operating variables. This slight difference might be related to the concentration polarization effect and it might become considerably more severe and significant at higher pressure loads on the RO membrane [42]. The increase in concentration polarization leads to the increase in osmotic pressure and the reduction of the driving force and eventually leads to a slight decline of the flux [35].

5.4.5. Dependence of permeate flux on feed flow rate and salt concentration

Fig. 10a demonstrates the graphical representation of the 3D surface and the corresponding contour of permeate flux determined experimentally and calculated theoretically and investigated with respect to the predicted results exhibited in Fig. 10b. The permeate flux is determined and calculated as a function of combined effects of feed flow rate and salt concentration at constant P_f (6.3 MPa) and T_f (34.6°C). Both theoretical and experimental values of permeate flux were observed to be increasing with an increase

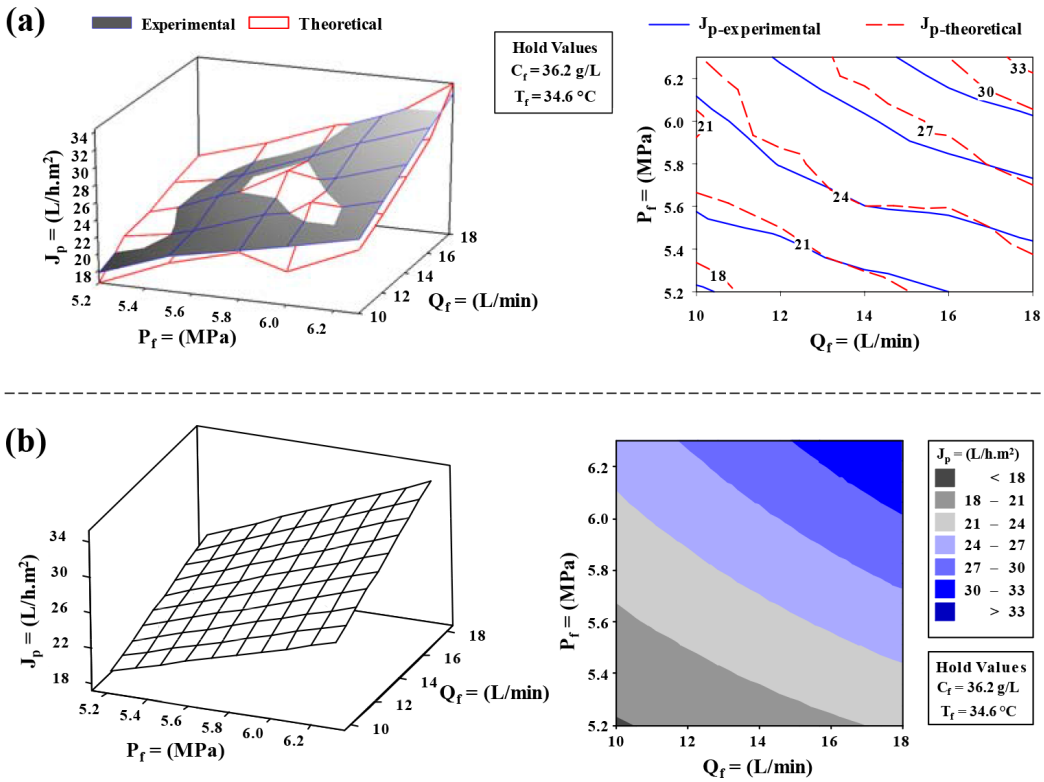

Fig. 9. 3D response surface and 2D contour plots of permeate flux as a function of Q_f *and* P_f: (a) Experimental and theoretical J_p, (b) Statistically predicted J_p.

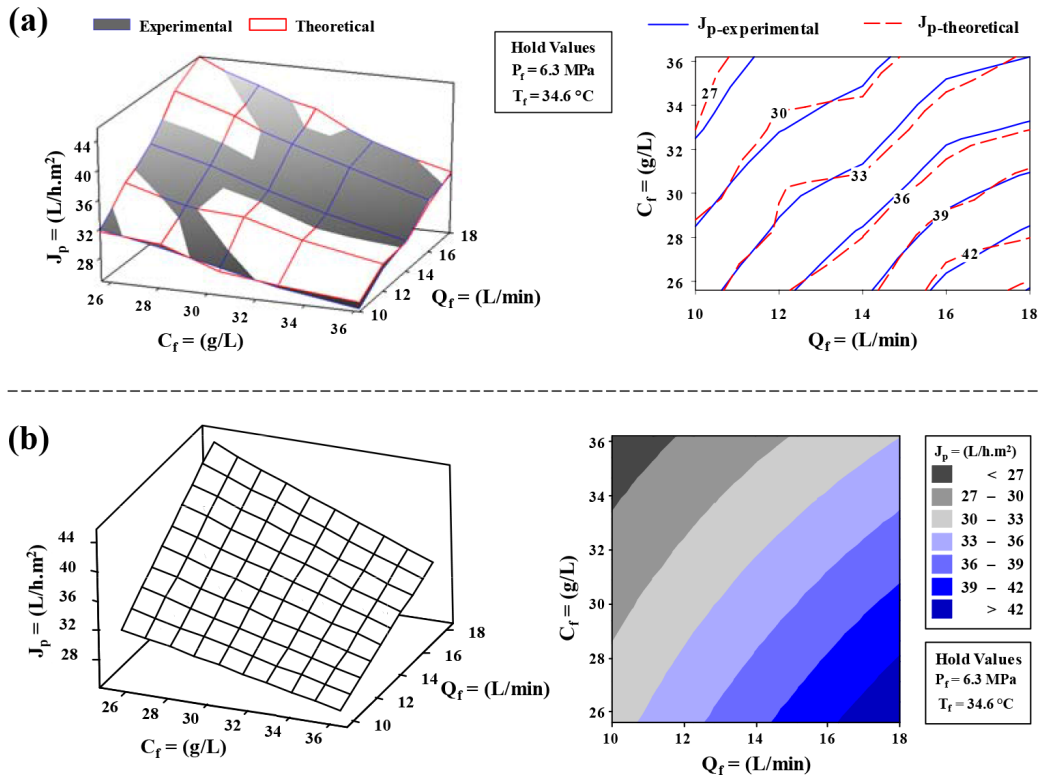

Fig. 10. 3D response surface and 2D contour plots of permeate flux as a function of Q_f *and* C_f: (a) Experimental and theoretical J_p, (b) Statistically predicted J_p.

of Q_f and decrease with an increase of C_f and the same trend was observed in case of predicted results. The permeate flux attained the maximum value when the RO unit operated at highest Q_f of 18 L/min and lowest C_f of 25.6 g/L. The reason being that the turbulence flow increases near the membrane surface resulting in decrease of solute concentration, thus leading to reduction of the concentration polarization and therefore, the permeate flux enhances. The permeate flux attains maximum values of 45.1 L/ h·m^2 and 44.9 L/ h·m^2 for experimental results and theoretical calculations, respectively. Both the 3D response surface and the 2D contour plot of permeate flux evidently indicates an exceedingly near agreement and trend for the theoretically calculated values to the experimental measurements. Within this experimental conditions and using the model equation, the maximum J_p obtained is 45.1 L/h·m^2.

5.4.6. Dependence of permeate flux on feed temperature and salt concentration

To evaluate the effect of feed temperature and salt concentration and their interaction with permeate flux, the graphical representation of the experimental results and theoretical calculations values are exhibited in Fig. 11a and compared with those obtained by the prediction model demonstrated in Fig. 11b. The results indicate that the permeate flux increases with increasing T_f and decreases with increasing C_f maintaining Q_f constant at 18 L/min and P_f at 6.3 MPa. According to these figures, the ideal operation conditions of RO system to maximize the permeate flux are to operate at a higher T_f combined with a lower C_f and attained a maximum value of 45.1 L/h·m^2 and 45.7 L/h·m^2 for the experimental values and theoretical calculations, respectively. Using the regression model of permeates flux [Eq. (19)], a maximum value of 45.1 L/h·m^2 was obtained. According to the 2D contour plot, the theoretical calculations of the permeate flux are observed to be in a satisfactory agreement with the experimental values.

5.5. Prediction of the J_p

Fig. 12a depicts the regression plot between the permeate flux measured from the experiments and the theoretically calculated values. It could be observed that the theoretical results are exceedingly near to experimental measurements. It could be observed that the major portion of the data concentrated towards the straight line and fall in this line. Moreover, the correlation coefficient R^2 is observed to be over 0.9786. This value confirms the satisfactory agreement between the experiments and the theoretically calculated values. According to Fig. 12a, the regression equations accurately follow the experimental results.

The regression function, which was generated using the experimentally measured results, was used to predict the permeate flux with confidence level of 95%. All the statistically significant primary effects and interaction effects were considered because of their high (>0.05) p-values based on the ANOVA results provided in Table 6. The regression function obtained is illustrated in Eq. (19). The quality of the developed model was estimated based on the correlation coefficient R^2 and the standard deviation values. The accuracy of the predicted response by the model could be evaluated by the proximity of its R^2 value to unity and the least value of its standard deviation. In this study, the R^2

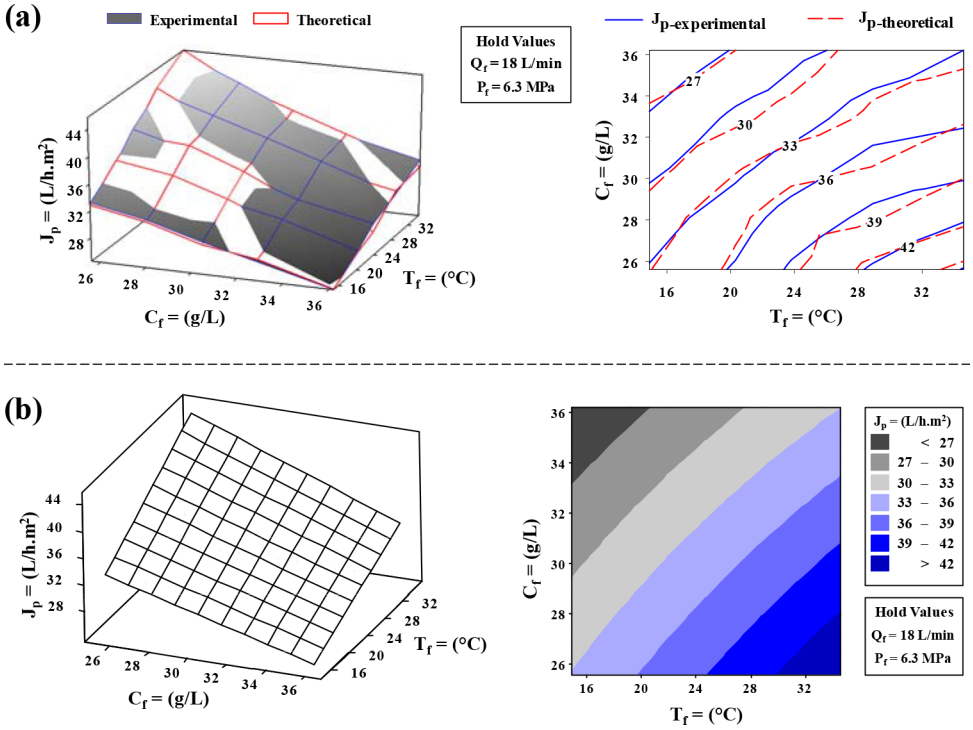

Fig. 11. 3D response surface and 2D contour plots of permeate flux as a function of T_f and C_f: (a) Experimental and theoretical J_p, (b) Statistically predicted J_p.

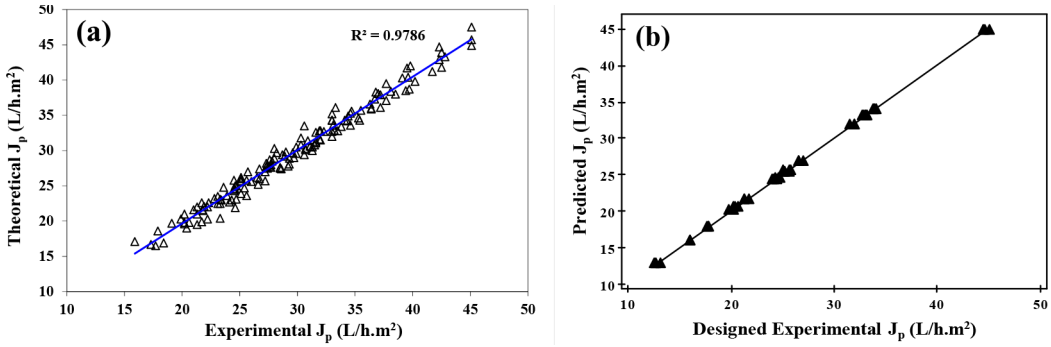

Fig. 12. (a) Theoretical J_p vs. Experimental J_p; (b) predicted J_p vs. Designed Experimental J_p.

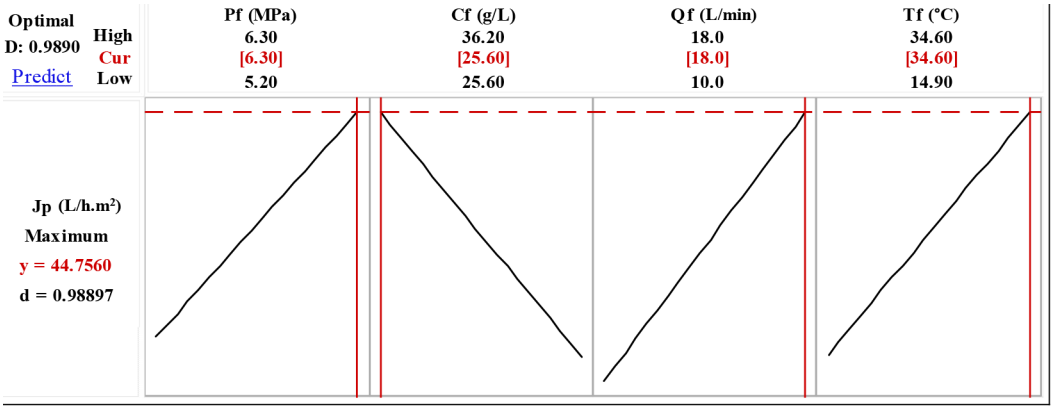

Fig. 13. Optimization plot for permeate flux.

and adjusted R^2 values for Eq. (19) were observed to be 0.999 which indicated that 99.9% of the total variation in the permeate flux was attributed to the input variables studied. Fig. 12b illustrates the comparison plot for the designed experimental and statistically predicted values of J_p. It could be seen evidently that there is a satisfactory agreement between the experimental and predicted J_p from the model, and hence the model could be considered as an adequate fit, confirmed by the regression equations that follow the experimental results with a satisfactory accuracy, since the R^2 value is nearly unity.

5.6. Optimization and performance investigation of the RO pilot plant

In DoE, response optimization is a method used to aid in identifying the combination of input variable settings that simultaneously optimize single/multiple responses. Individual desirability (d) evaluates how a single response is optimized by the settings. It uses a desirability function (DF) to assess how suitably the input variables cumulatively satisfy the goals that are defined for the responses. It has weight ranging from zero to one to determine how much to emphasize reaching the target value. If one or more responses are in a range away from their acceptable limits, it is indicated by zero and one implying the ideal case [29]. In this study, based on two-level factorial design, optimization was conducted to maximize the response. To achieve maximum desirability, P_f, Q_f, C_f *and* T_f were set within the range, whereas J_p was set to the maximum level. The software calculates an optimal solution by determining the optimal settings for input variables and to maximize the desirability and infers a plot. Fig. 13 illustrates the graphical representation of desirability generated from the optimum range of the combined variables. At the ideal range with maximum overall desirability of 0.988, the optimum P_f, C_f, Q_f *and* T_f were observed to be 6.3 MPa, 25.6 g/L, 18.0 L/min and 34.6°C, respectively. Under the optimum conditions, permeate flux of 44.756 L/h·m² is obtained. This optimal solution from the plot is the introductory point such that it allows interactively changing the input variable settings in the optimization plot to perform sensitivity analyses and for further possible improvement of the initial solution.

6. Conclusion

An extensive theoretical, experimental and statistical comparison study for the performance of RO unit is presented. The effect of the RO operating variables including the operating pressure (P_f, 5–6.3 MPa), salt concentration (C_f, 25.6–36.2 g/L), feed flow rate (Q_f, 14.9–34.6°C) and feed temperature (T_f, 10–18 L/min) on the permeate flux (J_p) were investigated to select the operating limits to conduct secondary experiments based on full factorial DoE methodology. The theoretical results based on the solution diffusion model were validated with the preliminary experimental

measurements using the 'one factor at a time technique' and a comparative analysis was conducted. DoE based secondary experimentation was conducted to develop full factorial empirical model such that comparison and validation analysis of the model predictions against experimental data and the theoretical calculations. All the statistically significant primary and interaction effects of the operating variables were examined and plotted on 3D response surface and 2D contour plots. The results indicated that the effect of operating pressure and feed flow rate were significant influencing factors at comparatively high feed water temperature on the permeate flux. Comparatively high permeate flux was obtained at lowest C_f value and correspondingly at highest P_f, Q_f *and* T_f values. The results confirmed that the salt concentration has negative effect on the permeate flux, whereas the other three factors, P_f, Q_f *and* T_f all have positive effects. The two-level full factorial technique was observed to be exceedingly effective for the prediction of permeate flux as the ANOVA results indicated an exceptional agreement, when comparing the experimental and the theoretical results with the model predictions at a high coefficient of determination (R^2) of 0.999 (with p-value <0.05). Process optimization was conducted to maximize the response using desirability function. At the ideal range with maximum overall desirability of 0.988, the optimum P_f, C_f, Q_f, *and* T_f were observed to be 6.3 MPa, 25.6 g/L, 18.0 L/min and 34.6°C, respectively.

Symbols

A_p — Water permeability coeff. ($m \cdot Pa^{-1} \cdot s^{-1}$)
A_{p0} — Constant in water permeability coeff.
B_s — Constant in water permeability coeff.
B_{s0} — Salt permeability coefficient ($m \cdot s^{-1}$)
C_f — Constant in salt permeability coeff.
CP — Salt concentration ($g \cdot L^{-1}$)
C_b — Concentration polarization
C_m — Membrane surface concentration ($g \cdot L^{-1}$)
C_p — Permeate salt concentration ($g \cdot L^{-1}$)
D_{AB} — Solute diffusion coefficient ($m^2 \cdot s^{-1}$)
d_h — Hydraulic diameter (m)
J_p — Permeate flux ($L \cdot h^{-1} \cdot m^{-2}$)
J_s — Salt flux ($L \cdot h^{-1} \cdot m^{-2}$)
k — Number of factors
k_c — Mass transfer coefficient ($m \cdot s^{-1}$)
P_f — Operating pressure (Pa)
DP — Trans-membrane pressure (Pa)
Q_b — Brine flow rate ($L \cdot min^{-1}$)
Q_f — Feed flow rate ($L \cdot min^{-1}$)
Q_p — Permeate water flow ($L \cdot h^{-1}$)
R — Universal gas constant ($Pa \cdot m^3 \cdot mol^{-1} \cdot K^{-1}$)
Re — Reynolds number
RR — Recovery ratio (%)
S — Effective membrane area (m^2)
Sc — Schmidt number
Sh — Sherwood number
SR — Salt rejection (%)
T_f — Feed temperature (°C)
u — Feed velocity ($m \cdot s^{-1}$)
X_i, X_j — Independent coded variables
Y — Response
π — Osmotic pressure (Pa)
ε — Experimental error
α — Solvent transport constant
ρ — Feed density ($kg \cdot m^{-3}$)
μ — Feed dynamic viscosity ($kg \cdot m^{-1} \cdot s^{-1}$)

Acknowledgements

The authors would like to thank the Engineering Faculties of University of Jeddah and King Abdulaziz University, KSA for providing the research facilities and encouragement.

Funding: This research did not receive any specific grant from funding agencies in the public, commercial, or not-for-profit sectors.

References

[1] M.A. Eltawil, Z. Zhengming, L. Yuan, A review of renewable energy technologies integrated with desalination systems, Renew. Sustain. Energy Rev., 13 (2009) 2245–2262.
[2] V.G. Gude, Energy consumption and recovery in reverse osmosis, Desal. Water Treat., 36 (2011) 239–260.
[3] C. Fritzmann, J. Löwenberg, T. Wintgens, T. Melin, State of the art of reverse osmosis desalination, Desalination, 216 (2007) 1–76.
[4] J.A.G.C.R. Pais, L.M.G. Ferreira, Estimation of stream compositions in reverse osmosis seawater desalination systems, Desalin. Water Treat., 1 (2009) 82–87.
[5] M. Pontie, J.S. Derauw, S. Plantier, L. Edouard, L. Bailly, Seawater desalination: nano filtration–a substitute for reverse osmosis?, Desal. Water Treat., 51 (2013) 485–494.
[6] R. Thiruvenkatachari, M. Francis, M. Cunnington, S. Su, Application of integrated forward and reverse osmosis for coal mine wastewater desalination, Sep. Purif. Technol., 163 (2016) 181–188.
[7] R.W. Baker, Membrane Technology and Applications, John Wiley & Sons, Ltd., Chichester, 2004.
[8] L.F. Greenlee, D.F. Lawler, B.D. Freeman, B. Marrot, P. Moulin, Reverse osmosis desalination: Water sources, technology, and today's challenges, Water Res., 43 (2009) 2317–2348.
[9] S. Sobana, R.C. Panda, Review on modelling and control of desalination system using reverse osmosis, Environ. Sci. Biotech., 10 (2011) 139–150.
[10] P.D. Gurak, L.M.C. Cabral, M.H.R. Leão, V.M. Matta, S.P. Freitas, Quality evaluation of grape juice concentrated by reverse osmosis, J. Food Eng., 96 (2010) 421–426.
[11] D.S. Couto, L.M.C. Cabral, V.M. Da Matta, R. Deliza, D.G.C. Freitas, Concentration of pineapple juice by reverse osmosis: physico chemical characteristics and consumer acceptance, Food Sci. Technol., 31 (2011) 905–910.
[12] J.M. Ochando-Pulido, A. Martinez-Ferez, Experimental design optimization of reverse osmosis purification of pretreated olive mill wastewater, Sci. Total Environ., 587–588 (2017) 414–422.
[13] H.U. Cho, K.H. Cho, S. Kang, Y.M. Kim, Optimization of operating variables in a pilot-scale reverse osmosis membrane process for reclamation of tunnel construction wastewater, Desal. Water Treat., 57 (2016) 12082–12089.
[14] M. Khayet, C. Cojocaru, M. Essalhi, Artificial neural network modeling and response surface methodology of desalination by reverse osmosis, J. Membr. Sci., 368 (2011) 202–214.
[15] A. Abbas, N. Al-Bastaki, Modeling of an RO water desalination unit using neural networks, Chem. Eng. J., 114 (2005) 139–143.
[16] S.M.J. Zaidi, F. Fadhillah, Z. Khan, A.F. Ismail, Salt and water transport in reverse osmosis thin film composite seawater desalination membranes, Desalination, 368 (2015) 202–213.

[17] N.M. A1-Bastaki, A. Abbas. Predicting the performance of RO membranes, Desalination, 132 (2000) 181–187.
[18] D. Hendricks. Fundamentals of water treatment unit processes: Physical, Chemical, and biological. Taylor & Francis Group, LLC, 2011.
[19] K. Jamel, M.A. Khan, M. Kamil, Mathematical modeling of reverse osmosis systems, Desalination, 160 (2004) 29–42.
[20] S. Kim, E.M.V. Hoek, Modeling concentration polarization in reverse osmosis processes, Desalination, 186 (2005) 111–128.
[21] B.A. Qureshi, S.M. Zubair, A.K. Sheikh, A. Bhujle, S. Dubowsky, Design and performance evaluation of reverse osmosis desalination systems: An emphasis on fouling modeling, Appl. Therm. Eng., 60 (2013) 208–217.
[22] B. Absar, O. Belhamiti, Modeling and computer simulation of a reverse osmosis desalination plant-case study of Bousfer plant-Algeria, Desal. Water Treat., 51 (2013) 5942–5953.
[23] A. Jiang, L.T. Biegler, J. Wang, W. Cheng, Q. Ding, S. Jiangzhou, Optimal operations for large-scale seawater reverse osmosis networks, J. Membr. Sci., 476 (2015) 508–524.
[24] H.J. Oh, T.M. Hwang, S. Lee. A simplified simulation model of RO systems for seawater desalination, Desalination, 238 (2009) 128–139.
[25] E.M.V. Hoek, J. Allred, T. Knoell, B.H. Jeong, Modeling the effects of fouling on full-scale reverse osmosis processes, J. Membr. Sci., 314 (2008) 33–49.
[26] P.P. Mane, P.K. Park, H. Hyung, J.C. Brown, J.H. Kim, Modeling boron rejection in pilot and full scale reverse osmosis desalination processes, J. Membr. Sci., 338 (2009) 119–127.
[27] M.S. Atab, A.J. Smallbone, A.P. Roskilly, An operational and economic study of a reverse osmosis desalination system for potable water and land irrigation, Desalination, 397 (2016) 174–184.
[28] A. Idris, F. Kormin, M.Y. Noordin, Application of response surface methodology in describing the performance of thin film composite membrane, Sep. Purif. Technol., 49 (2006) 271–280
[29] Minitab 17 statistical software. State College, PA: Minitab, Inc., 2013. Retrieved from www.minitab.com.
[30] D.C. Montgomery, Design and analysis of experiments, John Wiley & Sons, Inc., 2008.
[31] J. Antony, Design of experiments for engineers and scientists, Butterworth-Heinemann, New York, 2003.
[32] M. Cheryan, Ultra filtration and Micro filtration Handbook, CRC Press, 1998.
[33] L.Y. Hung, S.J. Lue, J.H. You, Mass transfer modeling of reverse-osmosis performance on 0.5–2% salty water, Desalination, 265 (2011) 67–73.
[34] M.J. Francis, R.M. Pashley, The effects of feed water temperature and dissolved gases on permeate flow rate and permeate conductivity in a pilot scale reverse osmosis desalination unit, Desal. Water Treat., 36 (2011) 363–373.
[35] H.U. Cho, K.H. Cho, S. KanG, Y.M. Kim, Optimization of operating variables in a pilot-scale reverse osmosis membrane process for reclamation of tunnel construction wastewater, Desal. Water Treat., 57 (2016) 12082–12089.
[36] H. Kotb, E.H. Amer, K.A. Ibrahim, On the optimization of RO (Reverse Osmosis) system arrangements and their operating conditions, Energy, 103 (2016) 127–150.
[37] M.F.A. Goosen, S.S. Sablani, S.S. Al-Maskari, R.H. Al-Belushi, M. Wilf, Effect of feed temperature on permeation flux and mass transfer coefficient in spiral-wound reverse osmosis systems, Desalination, 144 (2002) 367–372.
[38] K. Thirugnanasambandham, V. Sivakumar, K. Shine, Optimization of reverse osmosis treatment process to reuse the distillery wastewater using Taguchi design, Desal. Water Treat., 57 (2016) 24222–24230.
[39] A. Jawor, E.M.V. Hoek, Effects of feed water temperature on inorganic fouling of brackish water RO membranes, Desalination, 235 (2009) 44–57.
[40] T.D. Nguyen, K. Chan, T. Matsuura, S. Sourirajan, Effect of shrinkage on pore size and pore size distribution of different cellulosic reverse osmosis membranes, Ind. Eng. Chem. Prod. Res. Dev., 23 (1984) 501–508.
[41] M. Pendergast, J. Nygaard, A. Ghosh, E. Hoek, Using nanocomposite materials technology to understand and control reverse osmosis membrane compaction, Desalination, 261 (2010) 255–263.
[42] K.L. Tu, L.D. Nghiem, A.R. Chivas, Boron removal by reverse osmosis membranes in seawater desalination applications, Sep. Purif. Technol., 75 (2010) 87–101.